Nanoscale Horizons

ROYAL SOCIETY OF CHEMISTRY

COMMUNICATION

View Article Online
View Journal | View Issue

Cite this: *Nanoscale Horiz.*, 2026, **11**, 1614

Received 17th July 2025,
Accepted 17th February 2026

DOI: 10.1039/d5nh00503e

rsc.li/nanoscale-horizons

Regenerative bone-targeted nanoparticles modulate osteoclast function

Vignesh K. Rangasami, [a] Cameron J. Moore, [a] Baixue Xiao[bc] and Danielle S. W. Benoit *[abc]

Osteoclasts are vital for maintaining bone health. Indeed, dysregulated osteoclast activity is linked to pathological conditions such as Paget's disease, osteoporosis, and impaired fracture healing. Despite their importance in bone regeneration, few biomaterial-based strategies have been developed to alter osteoclast recruitment, differentiation, activity, or crosstalk with osteoblasts. To improve bone healing, we previously developed a drug delivery system (DDS) that expedites fracture repair. The DDS is composed of poly(styrene-*alt*-maleic anhydride)-*block*-poly(styrene) (PSMA-*b*-PS) functionalized with a peptide with inherent specificity to tartrate-resistant acid phosphatase (TRAP), a protein deposited by osteoclasts after bone injury (fracture, non-union, *etc.*). When loaded with a Wnt/β-catenin agonist (AR28), the TRAP binding peptide (TBP)-functionalized nanoparticle (TBP-NP$_{AR28}$) enhanced fracture healing by promoting pro-regenerative polarization of macrophages, enhancing osteogenic differentiation, and expediting fracture healing. Given their crucial role in bone healing and proximity during fracture repair, here we investigated the impact of NP on osteoclasts. Murine bone marrow-derived osteoclasts treated with NPs exhibited decreased osteoclastogenesis due to downregulation of key osteoclast genes (NFATc, cFOS, and CTSK) and function as assessed by reduced bone resorption capacity. The inhibition of osteoclastogenesis and the reduction in osteoclast function demonstrated here suggest that TBP-NP$_{AR28}$ is a promising approach for improving bone regeneration by combining osteoclast inhibition with its previously reported effects on bone formation. This offers new therapeutic strategies for bone diseases characterized by dysregulation of bone homeostasis.

New concepts

Fracture healing is a complex process involving various cell types, including mesenchymal stem cells, macrophages, osteoblasts, and osteoclasts. We previously showed that poly(styrene-*alt*-maleic anhydride)-*block*-poly(styrene) (PSMA-*b*-PS)-based nanoparticles (NPs) conjugated with tartrate-resistant acid phosphatase (TRAP) binding peptide (TBP) and loaded with the Wnt/β-catenin agonist AR28 enhance fracture healing by promoting macrophage polarization to the regenerative phenotype. Here, we demonstrate that these NPs also inhibit osteoclastogenesis and decrease osteoclast bone resorption. By playing a dual role of promoting the osteogenic milieu and reducing osteoclastic activity, these NPs can not only improve bone regeneration but also serve as potential therapies for osteoporosis and other conditions characterized by excessive osteoclastic activity.

Introduction

Bone is a dynamic tissue that protects vital organs, provides mechanical support for the body, enables movement, and serves as a reservoir for calcium, phosphate, and other essential minerals. Bone is also highly regenerative,[1] with the osteoclast–osteoblast axis crucial for healing.[2] However, 5–10% of all bone fractures still fail to heal or exhibit delayed healing.[3,4] Several risk factors, including gender, age, and other comorbidities, can contribute to impaired fracture healing. Among these, age is the most important factor. Osteoblasts and marrow stromal cells decrease in number and function with age, and the robustness of vascularization, which is crucial for healing, also diminishes.[5] The persistent inflammation, or inflammaging, typical of aged individuals also disrupts the osteoclast–osteoblast axis, increasing the number and activity of osteoclasts,[6] leading to delayed fracture healing and the development of age-related bone diseases, such as osteoporosis.[7] Hence, osteoclasts are implicated in impaired fracture healing[8,9] and the progression of osteoporosis.[10,11]

Current therapeutic interventions for bone-related disorders are generally divided into two categories: anti-catabolic (or anti-

[a] *Department of Bioengineering, Phil and Penny Knight Campus for Accelerating Scientific Impact, University of Oregon, Eugene, OR, USA. E-mail: dbenoit@uoregon.edu*
[b] *Department of Biomedical Engineering, University of Rochester, Rochester, NY 14623, USA*
[c] *Center for Musculoskeletal Research, University of Rochester Medical Center, Rochester, NY 14623, USA*

resorptive) and anabolic (or bone-forming) agents. Among the anti-resorptive drugs, bisphosphonates are the most common therapeutic option for managing osteoporosis and other bone diseases characterized by increased bone resorption.[12] Recently, a small-molecule inhibitor of cathepsin K, odanacatib, has shown promise in reducing fractures and increasing bone volume in early clinical trials by inhibiting bone resorption.[12] Teriparatide and romosozumab are among the anabolic drugs approved for bone regeneration. Teriparatide, a synthetic form of human parathyroid hormone, increases bone formation by promoting osteoblast activity.[13] Romosozumab, a humanized antibody, binds to sclerostin, a negative regulator of Wnt/β-catenin signaling, to promote bone formation.[13] However, most of these therapies have significant side effects, such as atypical femoral fractures (bisphosphonates) and strokes and cardiovascular events (odanacatib and romosozumab), that limit their use.[12,14]

To address the side effects of current bone-acting therapeutics, nanoparticle-based drug delivery systems (DDS) have been developed. Inorganic nanoparticles, such as gold and hydroxyapatite (HAp)-coated superparamagnetic iron oxide nanoparticles, have been used to treat osteoporosis.[15] For example, gold nanoparticles functionalized with β-cyclodextrin-curcumin complexes and alendronate-conjugated gold nanoparticles demonstrated the ability to reduce osteoclast formation and bone resorption in both *in vitro* and *in vivo* models.[16,17] HAp-coated iron oxide NPs were reported to promote osteoblastic differentiation of mesenchymal stem cells and inhibit osteoclast differentiation *in vitro*, while also preventing bone loss in an osteoporotic mouse model.[18] Lipid nanoparticles targeted with oligomers of aspartate (D-Asp8) to deliver the antagomir-148a (a microRNA modulator suppressing osteoclastogenic miR148a) have been used to reduce bone resorption, and PLGA/chitosan/alendronate-based polymer nanoparticles with high affinity for bone have shown promise for treating osteoporosis.[19,20] While promising, these therapeutic approaches are either anabolic or anti-catabolic, many clinical studies are currently exploring combinations of anabolic and anti-catabolic drugs to maximize treatment efficacy.[21]

We previously reported that poly(styrene-*alt*-maleic anhydride)-*block*-poly(styrene) (PSMA-*b*-PS) nanoparticles increase the accumulation of small-molecule drugs at the fracture site when targeted with tartrate-resistant acid phosphatase binding peptide (TBP).[22] Owing to TBP, enhanced fracture-targeted localization and expedited fracture healing are observed when the DDS delivers the Wnt/β-catenin agonist, AR28.[22,23] Further investigation revealed that our DDS enhanced bone regeneration by promoting the pro-regenerative polarization of macrophages, leading to more robust recruitment and proliferation of osteoprogenitor cells, deposition of fracture callus, and remodeling into hard callus compared to controls.[23] In this study, we investigate the impact of AR28-loaded TBP-NPs (TBP-NP_{AR28}) on osteoclasts, which are also in close proximity during fracture healing and play a pivotal role in the bone remodeling phase of fracture healing.

Materials and methods

Polymer synthesis and characterization

Deionized water used in all studies had a resistivity of $\geq$18 MΩ. The solvents used in all studies were at >98% pure. Poly(styrene-*alt*-maleic anhydride)-*block*-poly(styrene) (PSMA-*b*-PS) was synthesized using reversible addition–fragmentation chain transfer (RAFT) as previously described.[23,24] Styrene (STY, ≥99%, ReagentPlus Sigma Aldrich) was purified through distillation, maleic anhydride (MA, Sigma Aldrich) was recrystallized from chloroform, and 2,2′-azo-bis(isobutyronitrile) (AIBN, Sigma Aldrich) was recrystallized from methanol. DCT was synthesized according to a previously established protocol.[23] In brief, *n*-dodecylthiol (Sigma Aldrich) was added dropwise to sodium hydride solution (Sigma Aldrich) in diethyl ether, followed by the addition of carbon disulfide and iodine. Following purification, the dried intermediate was reacted with 4,4-azobis(4-cyanopentanoic acid) in ethyl acetate under reflux conditions. The final product was obtained by recrystallization using hexanes. Notably, the copolymerization of styrene and maleic anhydride forms a well-defined and predictable alternating copolymer due to their relative reactivities. Maleic anhydride, with an electron-deficient vinylic group, preferentially reacts with the electron-rich vinylic group on styrene, and *vice versa*. This is documented in both non-controlled free radical polymerization and controlled (living) polymerization techniques, such as reversible addition–fragmentation chain transfer.[25,26] Leveraging this phenomenon, PSMA-*b*-PS diblock copolymers were synthesized in a one-pot polymerization with excess styrene to maleic anhydride (4 : 1 [STY] : [MA]) in the presence of chain transfer agent (CTA) 4-cyano-4-[(dodecylsulfanyltrithiocarbonyl)sulfanyl] pentanoic acid (DCT) (100 : 1 [MA] : [CTA]). The radical initiator (AIBN) was used (10 : 1 [CTA] : [initiator]) in dioxane [57% (w/w)], and the reaction mixture was purged with nitrogen over ice for 2 h before being placed in a 60 °C oil bath for 96 h. Under these conditions, the PSMA block is synthesized first as the maleic anhydride is consumed in a 1 : 1 ratio with respect to styrene, leaving only styrene monomers left to form the second PS homopolymer block.

After 96 h, the reaction mixture was exposed to air, then dissolved in acetone, after which it was precipitated twice with chilled petroleum ether (Fisher Scientific). The precipitated polymers were then dried under vacuum overnight. To verify the presence of the alternating PSMA block and the PS block, ^{13}C NMR was performed (50 mg mL^{-1}, acetone-D6, 8000 scans, delay time of 6 seconds, Bruker 300 MHz NMR). Perfectly alternating maleic anhydride-styrene-maleic anhydride (MSM) triads are observed based on the quaternary carbon shifts between 136 and 140 ppm. In contrast, a minor peak was observed for the maleic anhydride-styrene-styrene/styrene-styrene-maleic anhydride (MSS/SSM) triads between 140 and 144 ppm. Additional poly(styrene) peaks (SSS triads) between 144 and 147 ppm were also observed.[27,28] Taken together, these findings suggest the PSMA block is perfectly alternating, with a transitional gradient segment followed by the poly(styrene) block. This is further supported by the PSMA backbone in the

^{13}C NMR found in the regions between 33 and 55 ppm[27] (Fig. S1A–C). The polymers were characterized using gel permeation chromatography (GPC). The number-average molecular weight (M_n), weight-average molecular weight (M_w), and polydispersity (D) were determined using GPC with the mobile phase dimethylformamide (DMF, Fisher Scientific) containing 0.05 M lithium chloride. The GPC measurements were taken on a Shimadzu 20A GPC system equipped with TSKgel SuperHM-N and complementary guard columns from Tosoh Bioscience. The column was operated at 60 °C, with a flow rate of 0.35 mL min^{-1}. Detection was performed using a miniDAWN TREOS light-scattering detector and a T-rEX refractive index detector, both from Wyatt Technology. The data obtained was analyzed by Astra version 7.3.2. A refractive index increment (dn/dc) of 0.142 mL g^{-1} was used to characterize all polymers, as previously determined.[24]

Peptide synthesis and characterization

Peptides were synthesized using the methods previously described.[24,29] Briefly, a Liberty Blue 2.0 synthesizer (CEM Corp.) was used to synthesize the TRAP binding peptide TBP-Alloc (TPLSYLKAllocGLVTVG) and the scrambled sequence peptide SCP-Alloc (VPVGTLSYLKAllocLTG). The lysine group in TBP and SCP was protected with an allylic (acid-resistant) group to ensure that only the terminal amine (and not the lysine amine) can participate in the conjugation reaction. Fluorenylmethyloxycarbonyl chloride (FMOC)-protected amino acids were used for the peptide synthesis. The individual amino acids used in the synthesis are listed in Table S3 of the SI. The coupling of amino acids (0.2 M) was achieved using an activator mix containing 1 M DIC (diisopropylcarbodiiamide) in dimethylformamide (DMF) and an activator base mix containing 1 M Oxyma in DMF. Deprotection of the individual amino acids during coupling was performed using 10% pyrrolidine in DMF. Following synthesis, the peptides were cleaved from Fmoc-Gly-Wang resin/Protide (CEM) using a mixture containing 92.5% trifluoroacetic acid (TFA), 2.5% water, 2.5% 3,6-dioxa-1,8-octanedithiol (DODT), and 2.5% triisopropylsilane (TIPS) for 30 min at 40 °C (CEM Razor- CEM). The peptides were then precipitated in cold diethyl ether and vacuum dried overnight. The successful synthesis was verified using matrix-assisted laser desorption/ionization using α-Cyano-4-hydroxycinnamic acid as matrix (Bruker Microflex Smart LS MALDI, Germany). The purity of the peptides was assessed by high-performance liquid chromatography (HPLC)[Shimadzu LC-20AD HPLC system, SPD-20AV ultraviolet-visible (UV-vis) detector]. HPLC was performed using a Kromasil C18 column (50 mm × 4.6 mm, 5 μm particle size, 100 Å pore size) with a variable wavelength UV-vis detector using the following parameters: flow rate of 0.5 mL min^{-1} from 95% to 10% A (0.1% TFA in HPLC grade water) and 5% to 95% B (HPLC grade acetonitrile) over 21 minutes.

Synthesis of peptide–polymer conjugates, self-assembly, and drug loading

The peptides were conjugated to the PSMA-*b*-PS *via* MA ring opening using nucleophilic addition–elimination.[24,29] Both PSMA-*b*-PS and the peptides were dissolved in DMF. Then, the peptides with a molar feed ratio of 10% on a diblock copolymer anhydride basis were added to the polymer solution and stirred at room temperature overnight. To remove any unreacted peptide and DMF, the polymer peptide conjugates were precipitated in cold diethyl ether. The resulting product was dried under vacuum overnight. Following this, the conjugates were analyzed for their molecular weight and polydispersity using GPC as described above. The number of peptides per polymer chain was calculated from the molar mass difference between PSMA-*b*-PS and the corresponding peptidyl conjugate, as described in our previous study.[24] Subsequently, deprotection of the Alloc group of lysine was performed as previously described.[29] Briefly, the polymer–peptidyl conjugates were dissolved in DMF and purged with nitrogen for 20 min. Tetrakis [Pd(PPh$_3$)$_4$, 0.25 N eq to peptide] was dissolved in 2 : 1 DMF : DCM and purged with nitrogen for 20 min. After this, the tetrakis was quickly added to the polymer–peptidyl solution, after which phenylsilane (25 eq. to peptide) was added, and the resulting solution was reacted for 20 min. Following this, the polymer–peptidyl solution was precipitated in 1 : 1 ice-cold diethyl ether : hexanes mixture. This reaction was repeated to ensure the complete removal of the Alloc protecting group. The polymer–peptidyl conjugates were then dialyzed against water in a 6–8 kDa MWCO dialysis membrane (Spectra Por) for 24 h, followed by lyophilization for characterization and downstream applications. The removal of the Alloc groups from the polymer–peptidyl conjugates was confirmed through ^{1}H NMR spectroscopy (Bruker 300 MHz) which was performed using deuterated DMSO (DMSO-d6) for 200 scans with a delay time of 4 s (Fig. S1D).

To form NPs, the polymer–peptidyl conjugates were dissolved in DMF at 6.7 mg mL^{-1} and ddH_2O was gradually introduced *via* a syringe pump at a rate of 24 μL min^{-1} using a 29.2 mm diameter 50 mL syringe. The resulting NP solution was then dialyzed against water for 3 days using a 6–8 kDa MWCO dialysis membrane (Spectra Por), after which it was filtered through 0.2 μm sterile cellulose acetate filters. Dynamic light scattering (DLS) was used to measure the hydrodynamic size and surface charge of the NPs utilizing a Malvern Zetasizer. The loading of GSK3β inhibitor AR28 [AZD2858; MedChemExpress (HY-15761)] was performed during the NP self-assembly. Briefly, 15 mL of ddH_2O was added to a mixture of AR28 (25 mg) and TBP-NPs (100 mg) in DMF using a syringe pump under conditions mentioned above. The resulting product TBP-NP$_{AR28}$ was dialyzed against water to remove DMF, as discussed above. For the loading estimation, a two-step method (A & B) was used to determine the total amount of drug loaded within TBP-NP$_{AR28}$ and was measured by HPLC. Step A: 100 μL of the drug-loaded NPs was collected from the bulk sample and diluted to 900 μL of acetonitrile. 10 μL of this is then injected into the HPLC through an autosampler. Step B: 100 μL of the bulk sample was collected, and free drug was separated from the drug-containing NPs using centrifugal filtration using Microcon YM10 centrifugal filters (Millipore, 10 kDa MWCO). These samples were centrifuged for 30 min at 6000 rpm, and

the free AR28 was measured from the filtrate after dissolution in acetonitrile as mentioned above. The drug loading and efficiencies were quantified by HPLC at a flow rate of 0.5 mL min^{-1}, from 90% to 30% A (0.1% TFA in HPLC grade water) and 10% to 70% B (HPLC grade acetonitrile) over 7 min. Drug loading efficiency and capacity were calculated as loaded drug/total drug × 100% and loaded drug mass/NP mass × 100%, respectively. To characterize the number of peptides per nanoparticle, a ZetaView Nanoparticle Tracking Analysis System from Particle Metrix was used. NPs at 0.01 mg mL^{-1} were filtered with 0.2 μm PES syringe filter and analyzed to determine the NP concentration (NP mL^{-1}). Together with peptides/polymer, as determined *via* GPC described above, and overall concentration used for analysis, the peptide/NP ratio was calculated.

Isolation of bone marrow cells and differentiation into osteoclasts

Osteoclasts are myeloid-derived cells. While myeloid cells can be isolated from various sources, cells for this study were obtained from bone marrow for ease of isolation and consistency. Bone marrow cells were isolated from the femurs of 8-to 15-week-old C57BL/6 mice and differentiated into osteoclasts using reported protocols.[30] Briefly, femurs were collected, washed with ice-cold phosphate-buffered saline (PBS), and the marrow was flushed out. The marrow cells were suspended in media (minimum essential medium α; αMEM; Gibco) supplemented with 10% fetal bovine serum (FBS; R&D Systems) and 1% penicillin/streptomycin (Gibco). The marrow cells were then passed through a 70 μm filter before being pelleted and resuspended in fresh culture e media. These bone marrow cells were cultured in flasks for 48 hours. After 48 h of mixed culture (mesenchymal and hematopoietic stem cells), the non-adherent cells (hematopoietic stem cells) were removed and differentiated into osteoclasts using osteoclast differentiation media (αMEM + 10% FBS+ 1% penicillin/streptomycin), supplemented with 20 ng mL^{-1} of macrophage colony stimulating factor (M-CSF; R&D Systems) and 40 ng mL^{-1} of receptor activator of NF-κB ligand (RANKL; R&D Systems). The media was replenished every 2–3 days and multinucleated cells were observed after 5–7 days of differentiation. The leukocyte acid phosphatase (TRAP) kit from Sigma Aldrich was used to stain for tartrate-resistant acid phosphatase (TRAP) deposited by the osteoclasts. Briefly, the cells were fixed with 4% paraformaldehyde for 15 min at room temperature. TRAP staining solution was prepared by mixing 50 μL of Fast Garnet's Base solution, 50 μL of sodium nitrite, 4.55 mL of distilled water, 50 μL of Napthol AS-Bisphosphate, 200 μL of Acetate solution, and 100 μL of tartrate solution. The fixative was aspirated, and the cells were washed twice with PBS, after which the TRAP solution was added. The cells were incubated in TRAP solution for 1 h at 37 °C. After 1 h, the cells were washed with distilled water before being observed under the microscope. The TRAP+ cells appear purple with three or more nuclei. The cells were imaged using a Leica Thunder fluorescence microscope. All animal procedures are approved by the University of Oregon's Institutional Animal Care and Use Committee (Id: IPROTO202200000265) and comply with the National Institutes of Health guide for the care and use of laboratory animals.

Cytocompatibility studies

Bone marrow cells derived osteoclasts were plated in 96-well plates and cultured for 24 h. The cells were then treated with TBP-NP and SCP-NP at concentrations between 0.01 mg mL^{-1} and 0.8 mg mL^{-1} for 48 h, after which the cells were washed with PBS. AlamarBlue reagent (ThermoFisher) was added directly to tissue-culture plastic adherent cells, followed by incubation at 37 °C for 4 hours to allow metabolic reduction of the dye. After incubation, fluorescence was measured (excitation/emission: 560/590 nm) using a BioTek Synergy H1 multimode plate reader, and the resulting signal was used to quantify cell viability. Cytocompatibility was also assessed using the alamarBlue reagent at TBP-NP_{AR28} concentrations ranging from 0 to 0.025 mg mL^{-1}, corresponding to 0–8 μM of AR28, based on the loading capacity reported in Table 1.

Nanoparticle uptake and flow cytometry

Nanoparticle uptake studies on the osteoclasts were performed using fluorescein-cadaverine conjugated TBP-NPs and SCP-NPs. Briefly, the NPs were reacted with 10 molar equivalents of fluorescein cadaverine in the presence of 10 molar equivalents of 1-ethyl-3-(3-dimethylaminopropyl)carbodiimide (EDC) relative to the polymer and 5 mM *N*-hydroxysuccinimide (NHS) for 2 h. The resulting product was then dialyzed against water for 24 h to remove unconjugated reactants. The fluorescein-conjugated NPs were stored in the dark until use. Bone marrow-derived osteoclasts were plated in 6-well plates and cultured for 24 h, after which they were treated with 0.1 mg mL^{-1} of fluorescein-conjugated TBP-NP and SCP-NP for a period of 1 h. The cells were washed with PBS, detached using Accutase together with gentle scraping, and subsequently resuspended in flow buffer (PBS supplemented with 3% FBS). The resulting

Table 1 Physicochemical properties of NPs used in this study. The molecular weights and PDI of the polymers, as well as peptides/polymer, were obtained by gel permeation chromatography (GPC). The size of NPs was measured using dynamic light scattering (DLS), and the drug loading efficiency and content were analyzed using high-performance liquid chromatography (HPLC). Nanoparticle tracking analysis was used to determine NP concentration. Combining these data with peptides/polymer, peptide density of the NPs was determined

NP	Block 1 (PSMA) M_n [kDa]	Block 2 (PS) M_n [kDa]	Diblock copolymer		TBP-diblock copolymer		Size (nm)	Zeta (mV)	PDI	Loading capacity (LC%)	Loading efficiency (LE%)
			M_n [kDa]	PDI	M_n [kDa]	PDI					
$TBP_{36\,000}$-NP	20	25	45	1.0	62	1.3	29 ± 5	−48 ± 4	0.2	—	—
$TBP_{36\,000}$-NP_{AR28}	20	25	45	1.0	62	1.3	36 ± 9	−41 ± 3	0.2	21% ± 2	86% ± 8

single-cell suspension was then analyzed using a Cytek Aurora spectral flow cytometer. To confirm internalization of NPs, 0.01% trypan blue (Sigma Aldrich) was added prior to the flow analysis. At low concentrations, trypan blue quenches green-emitting fluorophores.[31] To characterize osteoclasts, antibodies against cell-surface osteoclast markers were used. Briefly, osteoclasts were plated in 6-well plates and cultured for 24 h with osteoclast differentiation media after which they were treated with 0.01 mg mL^{-1} of TBP-NP and 0.01 mg mL^{-1} of TBP-NP_{AR28} for 10 days. The concentration of TBP-NP_{AR28} (0.01 mg mL^{-1}) was selected based on the loading capacity of AR28 ($\sim$21%, Table 1) that corresponded to an effective AR28 concentration of 1 μM, a dose previously proven to effectively activate the Wnt/β-catenin signaling pathway.[32] After 10 days, the cells were washed with PBS harvested and stained for cell surface osteoclast markers. Specifically, the cells were first treated with 2.5 μg mL^{-1} of Fc Block (CD16/CD32 monoclonal antibody; Fisher Scientific) for 15 min on ice and then stained with 5 μg mL^{-1} of CD9 (CD9-PE/Cy7; Biolegend), CD51/61 (CD51/61-FITC; Antibodies), CD265 (CD265-PE; ThermoFisher), and CD63 (CD63-APC; Biolegend) for 30 min at room temperature. The cells were then washed 3 times with PBS and resuspended in flow buffer and analyzed on the Aurora Spectral flow cytometer. CD9 + CD51/61- cells were classified as early osteoclasts and CD9 + CD51/61+ cells were classified as mature osteoclasts, as reported in literature.[33]

Gene expression studies

qRT-PCR was performed on the osteoclast before and after treatment to evaluate the effect of the NPs at the gene expression level. Gene expression levels of Cathepsin-K (CTSK), cFOS, ATPase H+ transporting V0 subunit d2 (ATP6V0d2) and nuclear factor of activated T-cells (NFATc) were analyzed, as they are known to be crucial in osteoclast maturation and osteoclastogenesis.[34] Specifically, osteoclasts cultured in osteoclast stimulation media were treated with 0.01 mg mL^{-1} TBP-NP and TBP-NP_{AR28} for periods of 3 days and 10 days. Untreated osteoclasts were used as controls. At the respective time points, the RNA from the cells was collected through TRIzol (ThermoFisher) RNA extraction method. After evaluating the quantity and quality of the extracted RNA using GE NanoVue Plus spectrometer. cDNA was generated using the qScript cDNA synthesis kit (Quantabio). PCR was performed using Perfecta SYBR Green SuperMix (Quantabio) to determine the gene expression levels of the osteoclast functional genes. Primer sequences were obtained from IDT Corporation and are listed in Table S4 (SI).

Bone resorption assay

To assess the effect of NP treatments on the bone resorption activity of osteoclasts, a bone resorption assay was performed using the Bone Resorption Assay Kit (Cosmo Bio).[35,36] The assay was performed according to the manufacturer's recommendations and allowed us to quantify bone resorption activity in a reproducible manner. Briefly, bone resorption assay fluoresceinamine-labeled chondroitin sulfate (FACS) was added to the assay plate and incubated at 37 °C for 1 h. The assay plate was then washed with PBS, and bone marrow-derived cells were added to the wells in phenol red-free α-MEM (Gibco) supplemented with 10% FBS, 20 ng mL^{-1} M-CSF, and 40 ng mL^{-1} RANKL. The cells were cultured for 3 days after which the media was replenished. TBP-NPs and TBP-NP_{AR28} were introduced to the respective groups at 0.01 mg mL^{-1} along with the media. Untreated cells were used as controls. 100 μL of the media was then transferred out every two days to a black 96-well plate, and the fluorescence intensity was measured with an excitation wavelength of 485 nm and emission wavelength of 535 nm using BioTek Synergy H1 Multimode reader.

F-actin ring staining

Rhodamine phalloidin reagent (ab235138) from Abcam was used to observe and stain the F-actin present in the osteoclasts. The manufacturer's instructions were followed to stain the F-actin. Briefly, Rhodamine Phalloidin conjugate (1000×) was diluted to 1× working solution in phosphate buffered saline (PBS). The cells cultured in chamber slides were fixed with 4% paraformaldehyde for 20 min at room temperature. The cells were then washed 2–3 times with PBS and 1× phalloidin conjugate solution is added to the cells. The cells were incubated at room temperature for 60 min, after which they were rinsed 2–3 times with PBS. Hoechst 33342 at 5 μg mL^{-1} was added to the cells and incubated for 15 min to stain the nuclei. The cells were then washed 2–3 times with PBS, after which ProLong Gold Antifade mountant was used to mount the coverslips. The cells were then imaged using a Leica TPS Sp8 confocal microscope.

The effect of NP-treated macrophage-conditioned media on osteoclasts

To study the influence of NP-treated macrophages on osteoclasts, macrophages (M0, M1, and M2) were treated with NPs, and the conditioned media from these cells were used to culture osteoclasts. Gene expression was then used to analyze the indirect influence of macrophages on the osteoclasts. Briefly, cells from C57BL/6 mice femurs were isolated and differentiated into M0 macrophages using 10 ng mL^{-1} M-CSF. Further differentiation into pro-inflammatory M1 macrophages was performed using 100 ng mL^{-1} lipopolysaccharides (LPS from *E.coli*; Sigma Aldrich) and anti-inflammatory M2 macrophages using 20 ng mL^{-1} of TGF-β, IL-10, and IL-4. These macrophages were then treated with 0.01 mg mL^{-1} of TBP-NP and TBP-NP_{AR28} for 48 h. The conditioned media from NP-treated macrophages was collected and used to culture osteoclasts in a 1 : 1 volumetric ratio with osteoclast media for up to 10 days [1 : 1 conditioned media from NP-treated macrophages: fresh osteoclast media (with stimulation factors)]. Untreated osteoclasts were used as controls. At the specified time points, RNA was isolated from the osteoclasts and qRT-PCR was performed, as described above.

RNA sequencing data analysis

To evaluate how nanoparticles influence bone regeneration after injury, we reanalyzed a previously generated RNAseq dataset derived from cells isolated from the fracture callus of mice treated with TBP-NP or TBP-NP_{AR28}.[23] Whereas the original study focused on NP-mediated changes in osteogenic programs, this secondary analysis was expanded to assess the effects of NP treatment on osteoclast-associated gene expression *in vivo*. Briefly, three days after mid-diaphyseal femur fractures were formed, treatments of saline, TBP-NP (18 mg kg^{-1} of polymer), and TBP-NP_{AR28} (5 mg kg^{-1} of AR28; 18 mg kg^{-1} of polymer) were introduced *via* retro-orbital injections. Mice were euthanized at days 1 and 7 after treatment, and cells were prepared for RNAseq as described previously.[23] Sequencing was performed on an Illumina HiSeq2500v4 high-throughput DNA sequencer at the University of Rochester Genomics Research Center, yielding ~35 million reads per sample. Raw reads generated from the Illumina base calls were demultiplexed using bcl2fastq version 2.19.1. Quality filtering and adapter removal were performed using FastP version 0.23.1. Processed/clean reads were then mapped to the GRCm39/gene code M31 or GRCh38/gene code 38 (mouse or human). Gene-level read quantification was derived using the subread-2.0.1 package (featureCounts) with a GTF annotation file (GRCm39/gene code M31 or GRCh38/gene code 42). iDEP.96 (https://bioinformatics.sdstate.edu/idep/), and DESeq2 was used to analyze the data set for the differential gene expression between the samples.[37,38]

Statistical analysis

Data are presented as mean ± standard deviation with sample sizes specified in the figure legends. GraphPad Prism was used for statistical analyses, employing one-way or two-way ANOVA, followed by Tukey's or Dunnett's *post hoc* testing, as indicated in the figure legends.

Results and discussion

We previously developed a bone-targeted drug delivery system using poly(styrene-*alt*-maleic anhydride)-*block*-poly(styrene) (PSMA-*b*-PS) nanoparticles functionalized with a tartrate-resistant acid phosphatase binding peptide (TBP). Through the introduction of TBP, there is approximately a threefold greater fracture accumulation of NPs conjugated with the targeting peptide when compared to scrambled peptide controls.[22] When used to deliver AR28, a Wnt/β-catenin agonist, expedited bone healing is observed compared to untreated controls. When the underlying mechanism was investigated, data initially suggested that improved bone regeneration was due to more robust osteogenesis in the regenerative stem cells, resulting from the upregulation of Wnt/β-catenin signaling.[22] However, further investigation revealed that TBP-NP_{AR28} promotes fracture healing and increases bone volume primarily by modulating macrophage phenotype.[23] Specifically, the anionic surface charge of TBP-NP_{AR28},[39] in conjunction with the bioactivity of AR28, promoted the polarization of macrophages towards a pro-regenerative phenotype. This shift resulted in an increased M2/M1 macrophage ratio at the fracture site, thereby promoting bone regeneration.[23] Given the complexity of the fracture microenvironment, which involves a coordinated cascade of cellular responses, the immunomodulatory effects of TBP-NP_{AR28} may also influence osteoclast activity, a key cell type in bone remodeling. This motivated the investigation into the impact of TBP-NP_{AR28} on osteoclast activity.

To this end, PSMA-*b*-PS diblock copolymers were prepared using a one-step reversible addition–fragmentation chain transfer (RAFT) polymerization of styrene and maleic anhydride (Fig. 1A). Gel permeation chromatography (GPC) revealed a molecular weight of 45 kDa and a low polydispersity (PDI) of 1.01 (Table 1 and Fig. S2 in SI), which is characteristic of RAFT polymerizations. The bone-targeting tartrate-resistant acid phosphatase-binding peptide (TBP) and a scrambled control peptide (SCP) were conjugated to the diblock copolymer maleic anhydride residues *via* ring-opening additions at molar feed ratios of 10% (Fig. 1B). GPC revealed molecular weights of 62 kDa and 57 kDa for the TBP- and SCP-conjugated diblock copolymers (Table 1 and Table S1, SI, respectively), which were used to estimate the number of peptides/polymer. The amine side chains of the lysine within the peptides, protected with an allylic group, were deprotected using tetrakis and phenylsilane, as described previously (Fig. 1C).[24,29] Once deprotected, the polymer–peptide conjugate was self-assembled into TBP-NPs through gradual addition of water (Fig. 1D). Characterization of these NPs through dynamic light scattering (DLS) revealed hydrodynamic diameter for TBP-NP of 29 ± 5 nm and surface Zeta potential of −48 ± 4 mV (Table 1). Nanoparticle tracking analysis was used to determine the NP concentration, which, together with the peptides/polymer chain and overall concentration used for analysis, was used to estimate the peptide/NP ratio.[24,29] These calculations revealed a peptide/NP of ~36 × 10^3 TBP ($TBP_{36\,000}$-NP) and ~ 27 × 10^3 SCP ($SCP_{27\,000}$-NP) per NP, as reflected in subscripts of Table 1, column 1 for TBP-NPs and Table S1 (SI) for SCP-NP. The Wnt/β-catenin agonist, AR28, was loaded into TBP-NPs during self-assembly to form TBP-NP_{AR28}. DLS characterization of the TBP-NP_{AR28} revealed a hydrodynamic diameter of 36 ± 9 nm and a Zeta potential of −41 ± 3 mV (Table 1). Further characterization by high-performance liquid chromatography showed that the TBP-NPs exhibited a drug loading efficiency of 86 ± 8% (loaded drug/initial drug) and a drug loading capacity of 21 ± 2% (drug mass/NP mass) (Table 1). Despite the 21% drug loading, nanoparticles largely retained their physicochemical properties, as evidenced by minimal changes in size and zeta potential following drug incorporation. The high drug loading capacity of the TBP-NP can be attributed to the hydrophobic, crystalline poly(styrene) core, which provides π-bonding groups complementary to AR28, aligning with our previous findings.[40,41] After self-assembly of SCP conjugated polymers into SCP-NPs, DLS characterization revealed a hydrodynamic diameter of 56 ± 7 nm and a Zeta potential of −51 ± 6 mV (Table S1, SI). This slight increase in the hydrodynamic size of the SCP-NPs may be

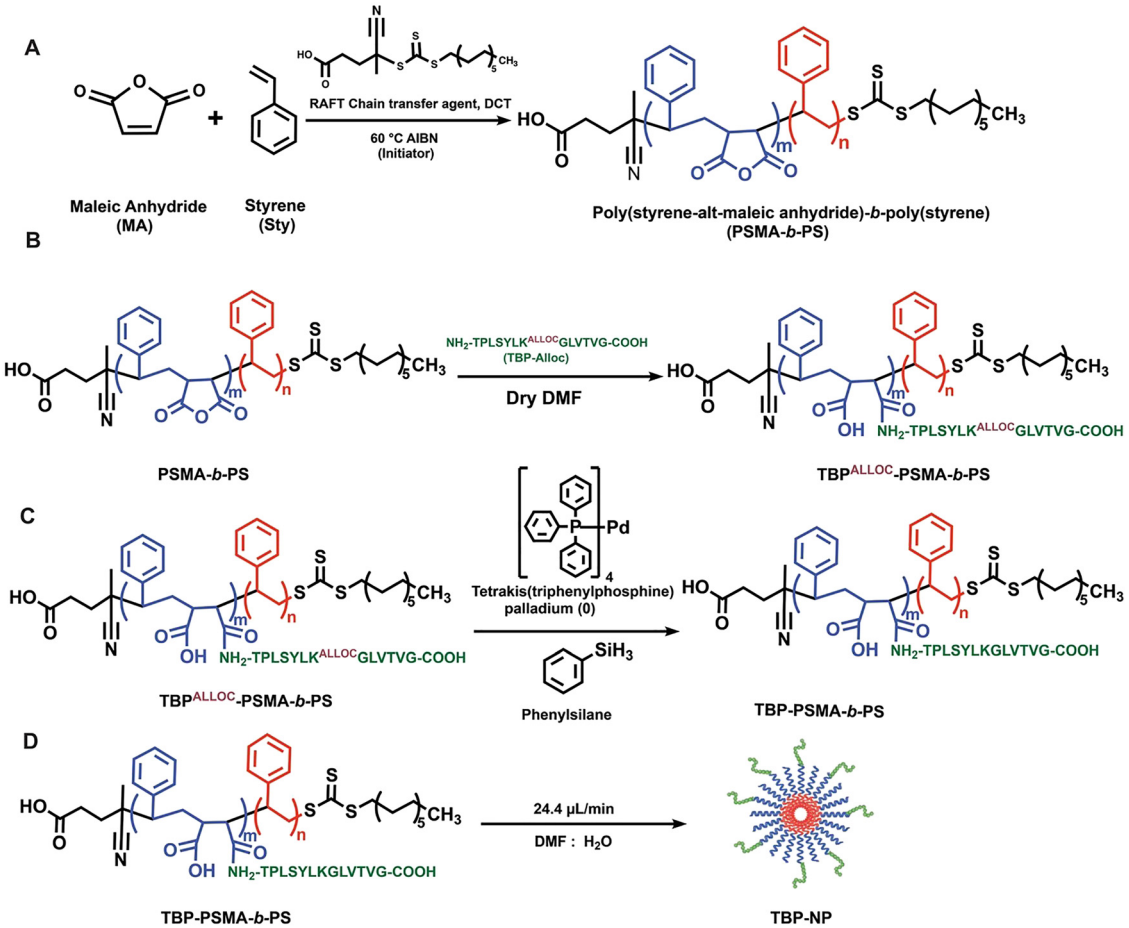

Fig. 1 Synthesis of the diblock copolymer (PSMA-*b*-PS), peptide-conjugated diblock copolymer, TBP-NP, and TBP-NP_{AR28}. (A) Poly(styrene-*alt*-maleic anhydride)-*b*-poly(styrene) polymer diblock was formed from maleic anhydride and styrene through reversible addition fragmentation chain transfer (RAFT) polymerization with 4-cyano-4-[(dodecylsulfanyltrithiocarbonyl)sulfanyl] pentanoic acid (DCT) as the RAFT chain transfer agent. (B) TRAP binding peptide (TBP) with an allylic group protecting the lysine amine group is conjugated *via* maleic anhydride ring opening. (C) After peptide conjugation, the allylic group is deprotected using tetrakis and phenylsilane. (D) The peptide-functionalized polymers are then self-assembled into NPs *via* solvent exchange.

due to the uneven distribution of hydrophobic amino acids, whereby SCP has a greater concentration at the N-terminus (Table S2, SI), which may influence the peptide extension from the NP surface, as previously observed through circular dichroism,[42] hydration, and, consequently, apparent NP size *via* DLS. Nevertheless, the overall size (<60 nm) and negative Zeta potentials are indicative of highly stable drug carriers with long drug-circulation half-lives, promising attributes for *in vivo* translation.[43]

To examine the effects of TBP-NP and TBP-NP_{AR28} on osteoclasts, bone marrow cells were isolated from the femurs of 8–15-week-old C57BL/6 mice. The bone marrow cells were differentiated into osteoclasts using macrophage colony-stimulating factor (M-CSF) and receptor activator of NF-κB ligand (RANKL), as previously reported.[30] After 5–7 days of culture, large multinucleated cells were observed, consistent with osteoclasts. As osteoclasts are known to produce high levels of tartrate-resistant acid phosphatase (TRAP), the phenotype of these large, multinucleated cells was confirmed through TRAP staining (Fig. 2A). To study the influence of NPs on osteoclasts, cytocompatibility was first assessed. Osteoclasts were treated with TBP-NPs at escalating concentrations (0.01–0.8 mg mL^{-1}) for 48 hours. In parallel, the cytocompatibility of the SCP-NPs was evaluated, with untreated cells serving as a control. We observed >70% cell viability of osteoclasts when treated with TBP-NPs at concentrations ranging from 0.01 mg mL^{-1} to 0.4 mg mL^{-1} (Fig. 2B). When treated with SCP-NPs, cell viability was greater than 70% at concentrations ranging from 0.01 mg mL^{-1} to 0.2 mg mL^{-1}. Both the TBP-NPs and SCP-NPs were cytocompatible at concentrations ranging from 0.01 mg mL^{-1} to 0.2 mg mL^{-1}, demonstrating >70% cell viability, per the ISO standard [ISO EN 10993–5].[44] Cytocompatibility was also assessed using TBP-NP_{AR28} at concentrations ranging from 0 to 0.025 mg mL^{-1}, corresponding to 0–8 µM of AR28, based on the loading capacity reported in Table 1. These data revealed that the TBP-NP_{AR28} is cytocompatible (cell viability >70%) at concentrations ≤0.01 mg mL^{-1} (Fig. S6A in SI).

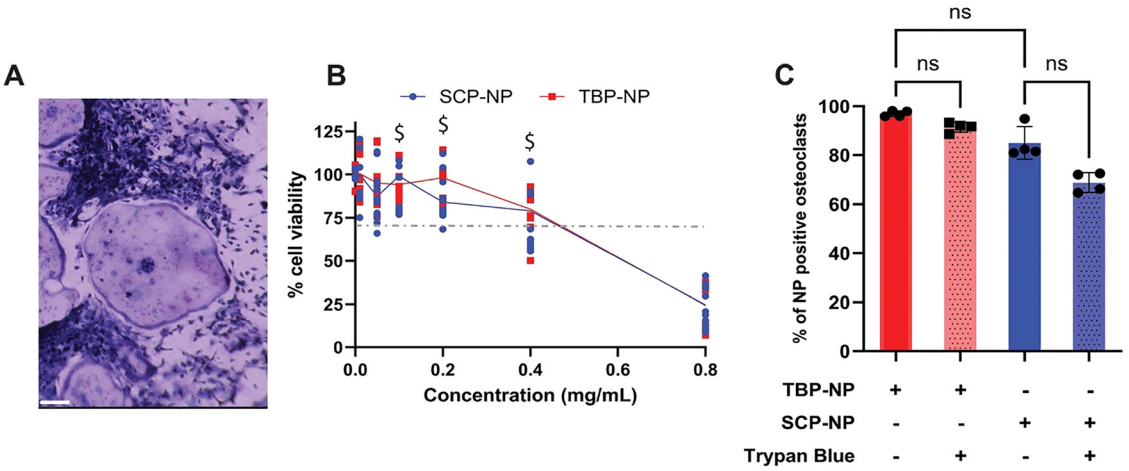

Fig. 2 Isolation of osteoclasts and NP cytocompatibility, uptake. (A) Cells from the bone marrow of mice (C57BL/6) were isolated and differentiated into osteoclasts, confirmed by TRAP staining. The purple stain indicates TRAP deposition. Scale bar represents 100 μm. (B) Cytocompatibility of TBP-NPs and SCP-NPs was assessed using the Alamar Blue assay. The dotted line shows 70% cell viability, which is the ISO standard for cytocompatibility. $N = 4$. Data are presented as mean ± standard deviation. Statistics were determined by 2-way ANOVA. $ = TBP-NP *vs.* SCP-NP, not significant. (C) Uptake of fluorescein conjugated TBP-NPs and SCP-NPs. Discrimination of internalized *versus* membrane-bound NPs was performed using trypan blue (TB) quenching of extracellular fluorescence. $N = 4$. Data are shown as mean ± standard deviation. Statistics were performed using the Kruskal–Wallis test. ns = not significant.

To assess nanoparticle (NP) uptake by osteoclasts, flow cytometry was performed on cells after treatment with 0.1 mg mL^{-1} fluorescein-labeled NPs for 1 hour, using trypan blue quenching to distinguish between internalized and cell-surface-bound NPs.[31] There was no significant difference in the cellular uptake of TBP-NPs and SCP-NP, with ~90% and 80% of cells positive for NPs, respectively, after 1 hour (Fig. 2C). Additionally, no significant difference in trypan quenching was observed, suggesting that all NPs were internalized. Since osteoclasts have significant phagocytic activity, comparable uptake of the targeted NP (TBP-NP) and the untargeted NP (SCP-NP) is unsurprising.[45]

After establishing the cytocompatibility and uptake of NPs by osteoclasts, the influence of NP treatment on osteoclast function was investigated. For this purpose, osteoclasts were treated with SCP-NPs, TBP-NPs, and TBP-NP_{AR28} for 3 and 10 days, respectively. While no changes were observed in TRAP deposition, morphological changes in osteoclasts were observed at later time points after NP treatment (Fig. 3A). Following treatment with TBP-NP and TBP-NP_{AR28}, fewer large multinucleated cells were observed. Instead, thin and spindle-like cells positive for TRAP were observed. A similar morphological change was observed in the osteoclasts after treatment with SCP-NPs, where the large multinucleated cells were replaced by thin spindle-like cells (Fig. S4A in SI). However, building on our previous findings that TBP-NP exhibits ~3-fold higher accumulation at the fracture site than untargeted NP,[22] we focused exclusively on TBP-conjugated NPs (TBP-NP and TBP-NP_{AR28}) for the remainder of these studies.

The morphological changes observed in osteoclasts prompted further analyses. Specifically, flow cytometry was used to investigate expression of osteoclast cell-specific surface markers (CD9, CD63, CD51/61, and CD265/RANK) after treatment with TBP-NP and TBP-NP_{AR28}. Tetraspanins CD9 and CD63 are involved in cell fusion processes, specifically in the formation of multinucleated giant cells (MGCs). Since osteoclasts are formed from the fusion of cells from the monocyte/macrophage lineage, they express high levels of CD9 and CD63.[46,47] CD265/RANK, which is induced by macrophage colony-stimulating factor (M-CSF), is associated with osteoclast differentiation and activity.[33] The expression of RANK triggers early activation of nuclear factor of activated T-cells, cytoplasmic 1 (NFATc1), which in turn sequentially transcribes osteoclast-specific late markers CD51/61, DC-STAMP, and TRAP.[48] As CD51/61 is a late marker, CD9 + CD51/61+ cells were classified as mature osteoclasts and CD9 + CD51/61- cells as early osteoclasts. After treatment of osteoclasts with TBP-NP and TBP-NP_{AR28}, no significant changes were observed in the proportion of cells that were CD9+ when compared to untreated controls (~80% controls; ~80% TBP-NP, and ~79% TBP-NP_{AR28}) (Fig. 3B). The proportion of CD63+ cells was approximately 40% lower after TBP-NP_{AR28} treatment compared to TBP-NP-treated cells (~77%) and untreated cells (~75%). Interestingly, the proportion of CD9 + CD51/61+ mature osteoclasts was lower after treatment with TBP-NP_{AR28} (~4%) than with TBP-NP (~5%) and untreated cells (~7%) (Fig. 3B). The lower number of mature osteoclasts corroborated the TRAP-stained images, as we observed a decrease in the number of large multinucleated cells after treatment with TBP-NP and TBP-NP_{AR28}.

The effect of the NPs on osteoclasts was further evaluated by examining the expression of genes involved in osteoclastogenesis and osteoclast activity (NFATc, CTSK, Atp6v0d2, and cFOS). NFATc, triggered in osteoclasts by the RANK/RANKL interaction, is known to translocate to the nucleus during late stages of osteoclastogenesis, promoting the expression of a multitude

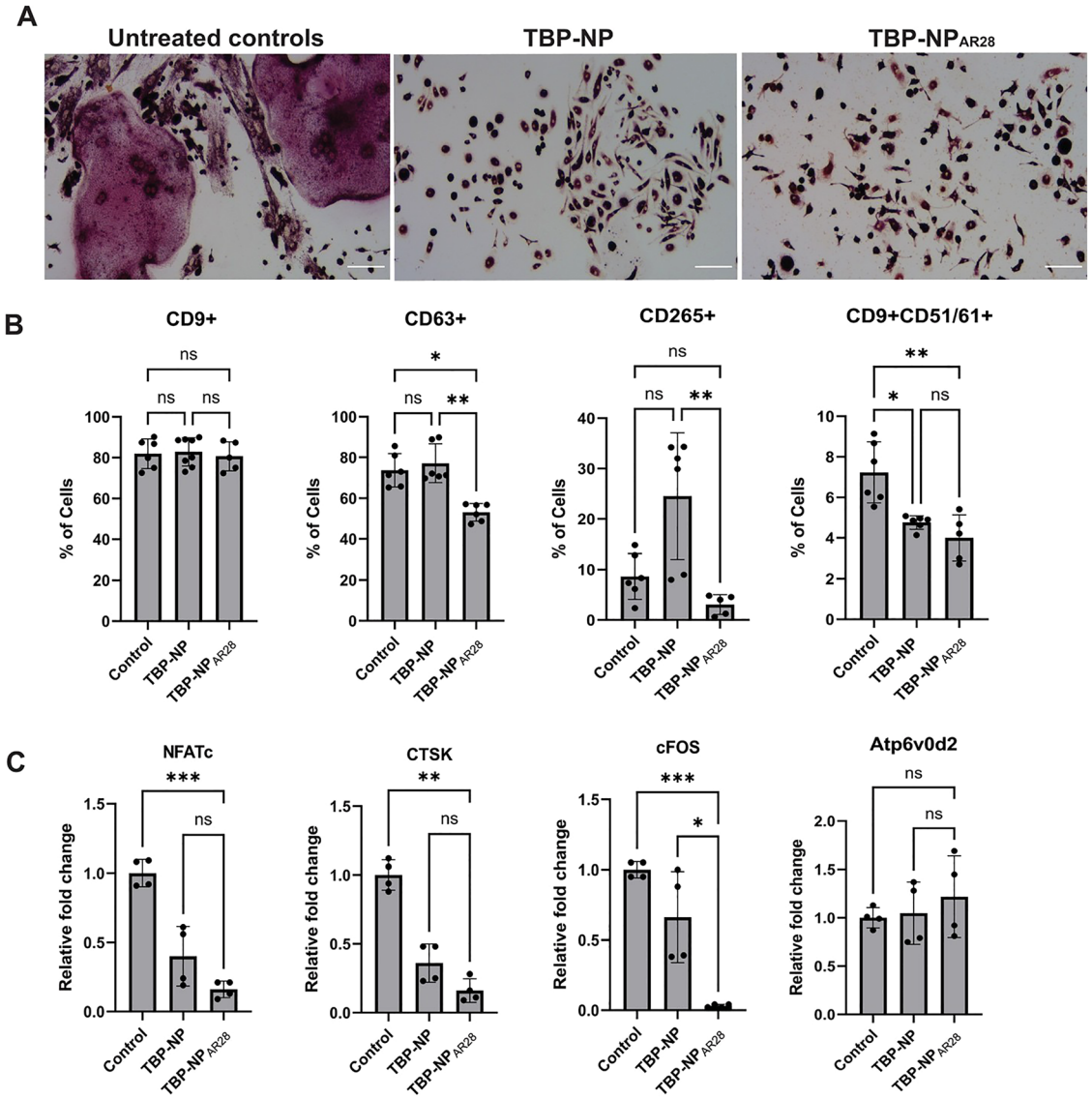

Fig. 3 NP treatment affects osteoclasts. (A) Morphological changes were observed when osteoclasts were treated with TBP-NP and TBP-NP_{AR28}. The scale bar represents 100 μm. Treatment of osteoclasts showed no change in TRAP deposited by the osteoclasts. (B) Flow cytometry analysis of osteoclasts after treatment with TBP-NP and TBP-NP_{AR28}. Control = untreated cells. Data are presented as mean ± standard deviation. $N = 3$. Statistical analysis was performed using Kruskal–Wallis test and Dunn's multiple comparisons. *$p < 0.05$, **$p < 0.01$. (C) Gene expression of genes involved in osteoclastogenesis and osteoclast function was analyzed by qRT-PCR after 10 days of treatment with TBP-NP and TBP-NP_{AR28}. Data are shown as mean ± standard deviation. $N = 2$. Statistical significance was determined by 2-way ANOVA and Dunnett's multiple comparisons test. *$p < 0.05$, **$p < 0.01$, and ***$p < 0.001$.

of osteoclast-specific genes involved in osteoclast activity and fusion.[49] cFOS, a member of the Activator protein-1 family, has been shown to regulate osteoclast differentiation by promoting NFATc and inhibiting osteoprotegerin.[49] The deficiency of NFATc and cFOS has been reported to impair osteoclast fusion and significantly reduce bone resorption activity in mice.[50,51] Osteoclasts secrete cathepsin K (CTSK) to degrade collagen during bone resorption, and its inhibition is known to decrease bone resorption while increasing bone formation.[52] Atp6v0d2, belonging to the family of vacuolar ATPase, is known to be highly expressed in osteoclasts. Reports suggest that depletion of Atp6v0d2 does not affect osteoclast fusion but impairs extracellular acidification and bone resorption, highlighting its role in osteoclast activity.[53]

mRNA levels of CTSK, cFOS, NFATc, and Atp6v0d2 were analyzed after treatment with TBP-NP and TBP-NP_{AR28} for 3 and 10 days. The mRNA levels of NFATc were 1.2-fold higher 3 days post-treatment with TBP-NP compared to untreated controls. However, 3 days after treatment with TBP-NP_{AR28}, a 0.3-fold reduction in the mRNA levels of NFATc was observed (Fig. S6B in SI). After 3 days of treatment with TBP-NP, CTSK mRNA levels did not differ significantly from those in untreated control cells, whereas cFOS mRNA levels increased 1.3-fold. However, a 0.3-fold and 0.1-fold reduction in CTSK and cFOS,

respectively, was observed 3 days post-treatment with TBP-NP_{AR28} (Fig. S6B in the SI). These data show that TBP-NP alone does not affect the mRNA levels of critical osteoclast genes; however, TBP-NP_{AR28} significantly reduced the mRNA expression of these genes. When mRNA levels were analyzed 10 days post-treatment with TBP-NP, significant reductions in mRNA expression of NFATc (0.4-fold), CTSK (0.4-fold), and cFOS (0.6-fold) were observed compared to untreated cells. (Fig. 3C). Ten days post-treatment with TBP-NP_{AR28}, 0.2-fold, 0.3-fold, and 0.1-fold reduction in the mRNA levels of NFATc, CTSK, and cFOS was observed compared to the untreated cells (Fig. 3C). While TBP-NP was effective in inhibiting these genes, TBP-NP_{AR28} was more potent. The increased potency of TBP-NP_{AR28} compared to AR28 is notable, as there have been reports where Wnt/β-catenin agonists, specifically GSK3β inhibitors, including lithium chloride and SB216763, have been shown to inhibit osteoclastogenesis by impairing the expression of NFATc.[54,55] Interestingly, no significant differences in Atp6v0d2 mRNA expression, a key regulator of bone resorption, were observed after treatment with either TBP-NP or TBP-NP_{AR28} compared with untreated cells.

The unaltered mRNA expression of Atp6v0d2, alongside the downregulation of NFATc, CTSK, and cFOS, prompted further investigation into the bone resorptive capacity of osteoclasts following treatment with NPs. For this purpose, bone resorption activity, as well as the formation of actin rings, were used to evaluate the impact of NP treatment on osteoclast activity. A commercially available kit from CosmoBio was used to analyze resorptive activity. The resorption assay revealed ~37% and ~45% lower osteoclast resorption activity after treatment with TBP-NP and TBP-NP_{AR28}, respectively, compared to untreated cells, corroborating the gene expression studies (Fig. 4A). To further confirm the reduction in bone resorption capabilities of osteoclasts after treatment with NPs, the formation of actin rings was observed. Bone-resorbing osteoclasts are known to have four distinct functional domains in their cell membrane. One of the functional domains is the clear zone, also known as the sealing zone.[56] The clear zone is often observed as actin rings, ring-like structures formed by F-actin dots. This zone, along with the ruffled border of the osteoclasts, is crucial for bone resorption as it helps in the formation of Howship's lacunae, which are maintained in an acidic state to dissolve hydroxyapatite and degrade matrix proteins of the bone.[56] It has been reported that actin rings of bone-resorbing osteoclasts appear to be thicker, larger, and more dynamic than the actin belt of non-resorbing osteoclasts on glass.[57] After treatment with TBP-NP and TBP-NP_{AR28} we observed the reduction in size and thickness of actin rings, when compared to the untreated osteoclasts (Fig. 4B-D). This suggests that, in addition to inhibiting key osteoclast genes, the

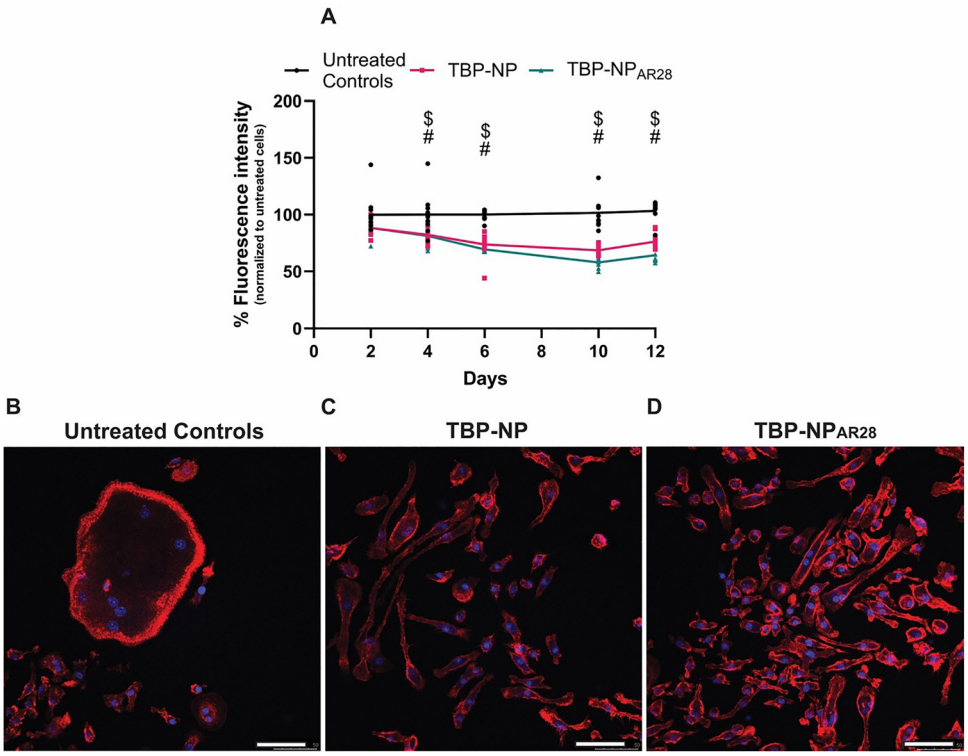

Fig. 4 Osteoclast bone-resorptive capabilities decrease after treatment with NPs. (A) Quantitative analysis of bone resorptive function following treatment with TBP-NP and TBP-NP_{AR28} was conducted using the Bone Resorption Assay Kit from CosmoBio. Data are expressed as mean ± standard deviation, with N = 2 and 6 replicates per condition. Statistics were analyzed using 2-way ANOVA and Dunnett's multiple comparison tests. $ = TBP-NP *versus* untreated controls $p < 0.01$, # = TBP-NP_{AR28} *versus* untreated controls $p < 0.01$. (B) Rhodamine-labeled Phalloidin was used to stain F-actin to visualize the actin rings, which are essential for bone resorption. (C and D) Actin staining showed fewer, larger sealing zones after treatment with NPs, indicating reduced resorption capacity. The scale bar represents 50 μm.

NPs significantly reduce the size of osteoclast actin rings, thereby impairing their ability to resorb bone. These findings are further supported by the bone resorption assay, which demonstrates that both TBP-NP and TBP-NP_{AR28} inhibit osteoclast bone-resorbing function.

To build on our previous findings that macrophages predominantly take up TBP-NP_{AR28} at fractures, influencing healing through pro-regenerative polarization,[23] we further investigated how NP-treated macrophages influence osteoclasts through paracrine signaling. Osteoclasts were treated with conditioned media collected from M0, M1, and M2 macrophages treated with TBP-NP_{AR28}, and the mRNA expression of critical osteoclast functional genes was assessed. When osteoclasts were treated with media of TBP-NP_{AR28}-treated macrophages, the mRNA levels of NFATc were showed no significant change at day 3 and ~0.6-fold reduction at day 10 after treatment with conditioned media from M0 macrophages when compared to untreated osteoclasts. Treatment of osteoclasts with conditioned media from M1 macrophages resulted in ~0.4-fold reduction of NFATc at both day 3 and day 10 (Fig. 5). A similar effect was observed with M2-conditioned media, where there was a ~0.6-fold reduction in NFATc mRNA levels at both days 3 and 10. There was a 0.2-fold, 0.2-fold, and 0.3-fold decrease in the mRNA levels of cFOS at day 3 after treatment with conditioned media from TBP-NP_{AR28}-treated M0, M1, and M2 macrophages, respectively, when compared to untreated cells (Fig. 5). At day 10 post-treatment, similar reductions of 0.3-, 0.3-, and 0.4-fold in cFOS mRNA levels were observed after treatment with conditioned media from TBP-NP_{AR28}-treated M0, M1, and M2 macrophages, respectively, compared to untreated cells (Fig. 5). A similar trend was observed with CTSK, where we observed 0.5-fold, 0.4-fold, and 0.5-fold reduction at day 3 and 0.4-fold, 0.4-fold, and 0.7-fold reduction at day 10 after treatment with conditioned media from TBP-NP_{AR28}-treated M0, M1, and M2 macrophages, respectively, when compared to untreated cells (Fig. 5). Interestingly, we observed a ~1.7-fold and ~2.2-fold increase in ATP6v0d2 mRNA levels at day 3 and a ~1.7-fold and ~2.4-fold increase at day 10 after treatment with conditioned media from TBP-NP_{AR28}-treated M0 and M2 macrophages, compared to untreated osteoclasts. Although ATP6v0d2 expression is upregulated, the simultaneous downregulation of NFATc1, a key transcription factor for osteoclast differentiation and bone resorption,[58] along with CTSK and cFOS, indicates that osteoclast function is compromised. Conditioned media from TBP-NP_{AR28}-treated M1 showed a 0.5-fold reduction in ATP6v0d2 mRNA at day 3 and day 10, compared to untreated controls. Reports indicate that both pro-inflammatory M1 macrophages and anti-inflammatory M2 macrophages can inhibit osteoclast function and osteoclastogenesis.[59,60] Here, after treatment with

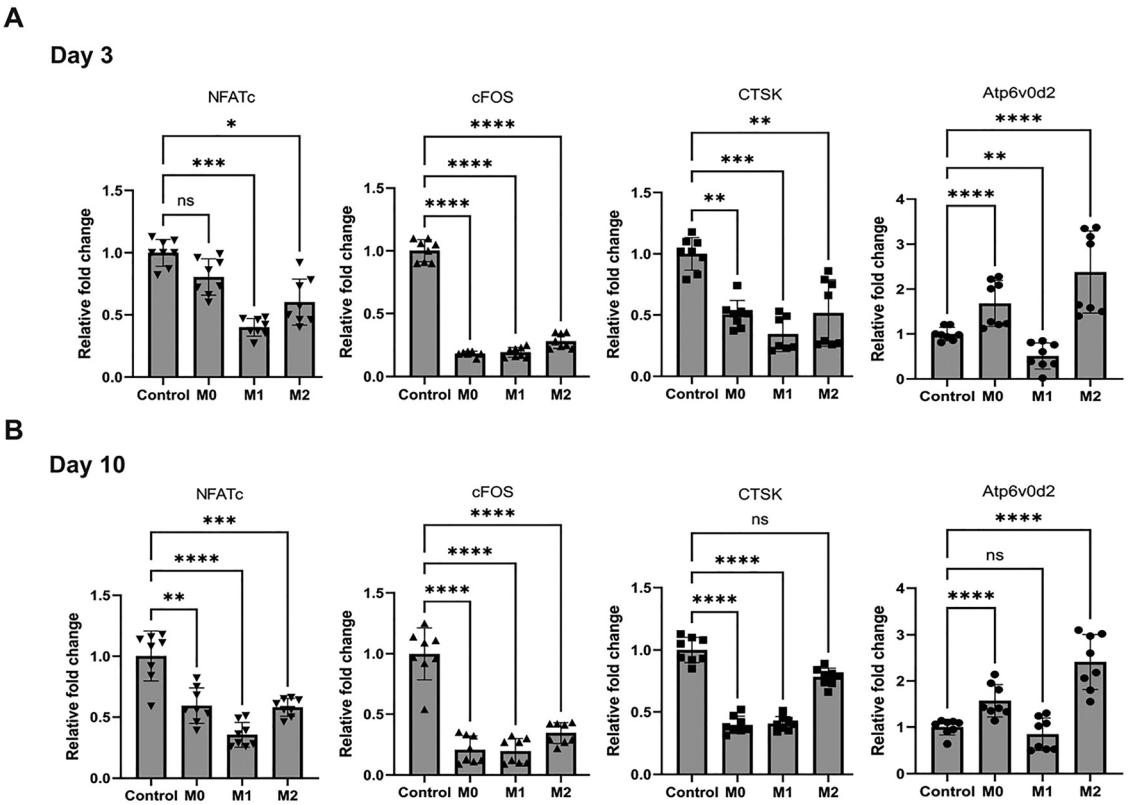

Fig. 5 Osteoclasts were treated with conditioned media from TBP-NP_{AR28}-treated M0, M1, and M2 macrophages. RNA was extracted from osteoclasts at (A) Day 3 and (B) Day 10 post-treatment with conditioned media, and qRT-PCR was performed to analyze the expression of NFATc, cFOS, CTSK, and AtpV0d2. $N = 2$, Control = untreated osteoclasts. Data are presented as mean ± standard deviation. Statistical significance was determined using 2-way ANOVA and Dunnett's multiple comparisons test. *$p < 0.05$, **$p < 0.01$, ***$p < 0.001$.

TBP-NP$_{AR28}$, macrophages inhibit osteoclastogenesis, as evidenced by reduced mRNA levels of CTSK, c-FOS, and NFATc in osteoclasts. Given that in the fracture microenvironment, macrophages predominantly uptake TBP-NP$_{AR28}$,[23] it is likely that subsequent macrophage paracrine signaling would not just promote osteogenesis but also inhibit osteoclast function, thereby contributing to enhanced bone regeneration after fractures.

To examine the effectiveness of TBP-NP and TBP-NP$_{AR28}$ in suppressing osteoclast function and promoting osteoblast activity *in vivo* at the gene expression level, a bulk RNA sequencing (RNA-seq) dataset was reanalyzed. Briefly, in a prior study, mice were treated with saline, TBP-NP, and TBP-NP$_{AR28}$ three days post-fracture.[23] Fracture-associated cells were collected at days 1 and 7 post-treatment for bulk RNAseq analysis. The top 2000 most variable genes across all groups and time points were clustered, and enrichment analysis was performed based on gene ontology (GO) biological processes and the kyoto encyclopedia of genes and genomes. Differentially expressed genes (DEGs) were then identified. Specifically, two clusters were enriched in biological processes associated with fracture healing, including bone development, ossification, endochondral bone morphogenesis, and extracellular matrix deposition. Biomarkers related to chondrogenic differentiation (such as cartilage oligomeric matrix protein (COMP), SRY-box transcription factor 6 (SOX5)) and osteogenic differentiation (integrin binding sialoprotein (IBSP), runt-related transcription factor 3 (RUNX3), bone morphogenetic protein 2 (BMP2)) were upregulated following treatment with TBP-NP$_{AR28}$. Further analysis of the top 30 DEGs revealed that 70% of the downregulated genes

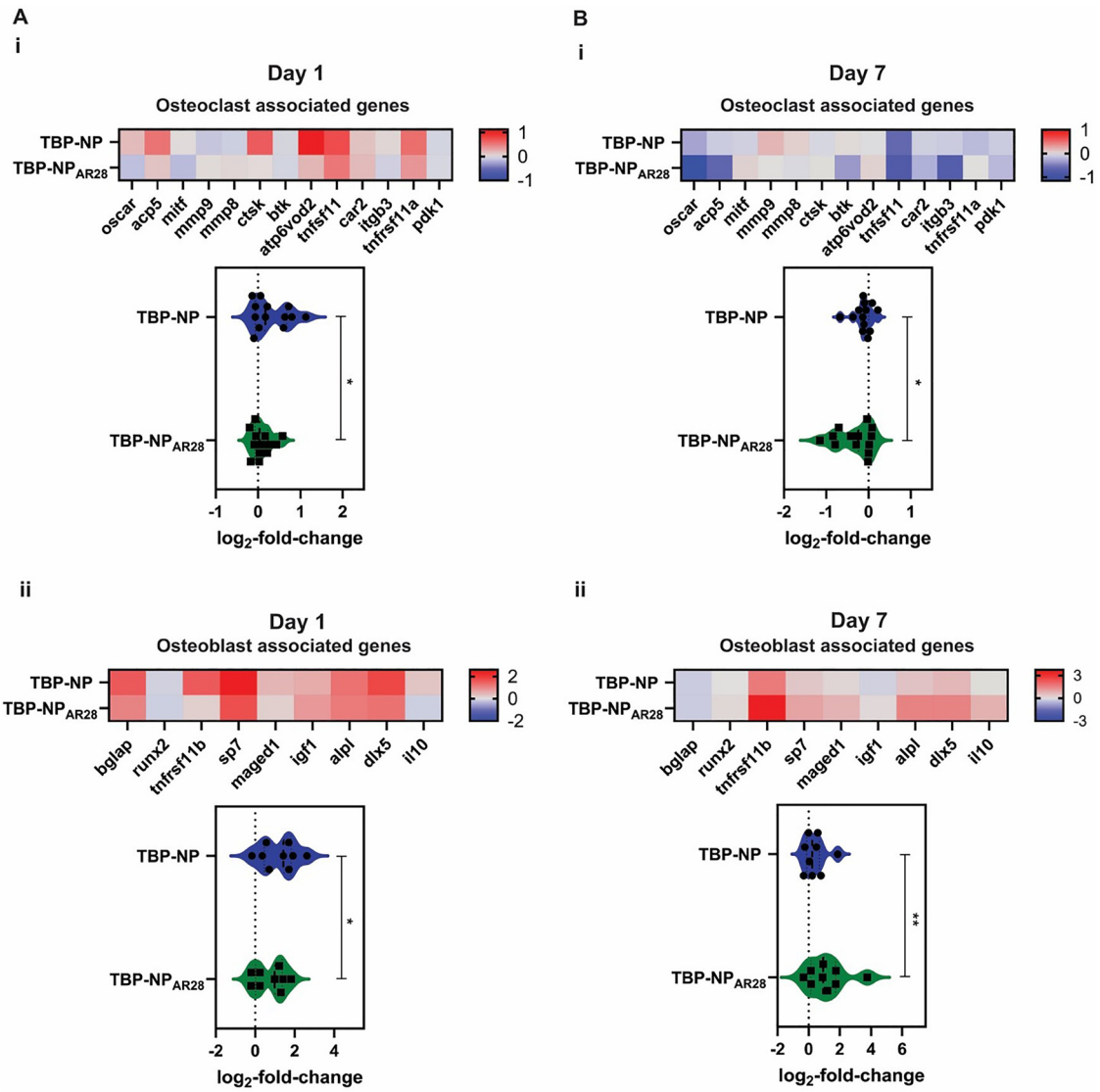

Fig. 6 Mice with femur fractures were treated with TBP-NP and TBP-NP$_{AR28}$, and differential expression of genes associated with osteoclasts and osteoblasts was obtained by bulk RNAseq at (A) day 4 and (B) day 10 post-treatment. Osteoclast-associated genes and overall osteoclast-associated gene expression at (A(i)) day 4 and (B(i)) day 10. Osteoblast-associated genes and overall osteoblast-associated gene expression at (A(ii)) day 4, (B(ii)) day 10. Scales indicate log$_2$-fold change. Statistics were performed using Student's *T*-test. *$p < 0.05$, **$p < 0.01$.

were associated with proinflammatory pathways, whereas 30% were related to anti-inflammatory pathways after treatment with TBP-NP_{AR28}, underscoring its advantages in fracture healing.[23] Upon re-examination of the DEGs, specifically those involved in osteoclast and osteoblast differentiation and function, cells treated with TBP-NP_{AR28} showed downregulation of osteoclast-associated genes and upregulation of osteoblast-associated genes compared to saline controls at day 7. As expected, the effect of TBP-NP_{AR28} was more pronounced at day 7 than at day 1 post-treatment (Fig. 6A and B). While there was a small effect of TBP-NP, a much more robust suppression of osteoclast gene expression was observed in cells isolated from TBP-NP_{AR28}-treated fracture callus (Fig. 6A and B). This more pronounced impact may be due to increased osteoprotegerin (OPG) production, triggered by AR28-induced activation of β-catenin, which GSK-3β inhibits.[23]

To support our claim that TBP-NP_{AR28} has a dual role, affecting both bone resorption and production, the expression levels of osteoclast- and osteoblast-associated genes were also examined. Among key osteoclast-associated genes, tartrate-resistant acid phosphatase (*acp5*)[61] and osteoclast-associated Ig-like receptor (*oscar*), which are required for osteoclastogenesis,[62] were downregulated by ~ -1 $\log_2$-fold change at day 7 post-treatment when compared to saline controls (Fig. 6 Bi). Similarly, integrin beta 3 (*itgb3*),[63] a key mediator of osteoclast adherence to bone surfaces, also exhibited ~ -1 $\log_2$-fold change at day 7 post-treatment compared to saline controls (Fig. 6B(i)). In addition, a similar ~ -1 $\log_2$-fold change in the expression levels of receptor activator of NF-κB ligand was observed [RANKL; (*tnfsf*11)], while the expression level of receptor activator of NF-κB [RANK (*tnfrsf*11*a*)] exhibited no change at day 7 post-treatment when compared to the saline controls (Fig. 6B(i)). The RANKL-RANK interaction is known to promote osteoclast differentiation, maturation, activation, and survival, leading to bone resorption.[64] Notably, osteoprotegerin [OPG, (*tnfrsf*11*b*)], a decoy of RANKL that inhibits its interaction with RANK, was upregulated by ~ 3 $\log_2$-fold change at day 7 post-treatment with TBP-NP_{AR28} (Fig. 6B(ii)). The biological effects of OPG (*tnfrsf*11*b*) released by osteoblasts are in direct opposition to RANKL and include inhibition of osteoclast differentiation, reduced osteoclast activity, and acceleration of osteoclast apoptosis.[64] Therefore, the reduction in the RANKL (*tnfsf*11) expression and the upregulation of OPG (*tnfrsf*11*b*) after treatment suggest that TBP-NP_{AR28} inhibits osteoclast differentiation and function.

Interestingly, both TBP-NP and TBP-NP_{AR28}-treated groups resulted in upregulation of osteoblast-associated genes at days 1 and 7 post-treatment (Fig. 6A(ii) and B(ii)). Osteocalcin (OCN; *bglap*), an early osteogenic marker,[65] was upregulated by ~ 2 $\log_2$-fold at day 1 post-treatment with TBP-NP and TBP-NP_{AR28}. Moreover, other osteoblast and bone formation markers[66] such as osterix (*sp*7), distal-less homeobox 5 (*dlx*5), and alkaline phosphatase (*alpl*) were upregulated by >1 $\log_2$-fold change at both days 1 and 7 after treatment with TBP-NP and TBP-NP_{AR28} (Fig. 6A(ii) and B(ii)). Collectively, these findings, in conjunction with our previously published work,[22,23] demonstrate that TBP-NP_{AR28} enhances fracture healing in mice by reducing osteoclast-associated genes and inducing osteoblast-associated genes, thereby confirming its dual-action mechanism.

Conclusions

This study explores the effects of a bone regenerative NP DDS on osteoclasts. We previously reported that TBP-NP_{AR28} accelerates fracture healing by promoting osteogenesis through macrophage polarization to a pro-regenerative M2 phenotype at the fracture site. Here, we show that TBP-NP_{AR28} also inhibits osteoclastogenesis and reduces osteoclast resorption. Specifically, treatment with TBP-NP and TBP-NP_{AR28} decreases the number of mature osteoclasts, as demonstrated by flow cytometry and gene expression analysis. Reduced osteoclast gene expression leads to reduced bone resorption, as observed in bone resorption assays and F-actin ring staining. Additionally, since fracture-associated macrophages take up NPs, TBP-NP_{AR28}-treated macrophages were shown to reduce key osteoclast functional genes through paracrine signaling. Importantly, RNA-seq analysis of fracture-associated cells confirms the inhibitory effects of TBP-NP_{AR28} observed *in vitro*, demonstrating consistent activity across osteoclast populations that may originate from different sources. Combined with their potential to promote fracture healing, these results suggest that TBP-NP_{AR28} could serve as a valuable therapeutic approach for managing various bone diseases caused by dysregulation of the osteoblast-osteoclast axis.

Author contributions

VR and DSWB conceptualized this work. VR, CJM, and BX were involved in the methodology and formal analysis. VR wrote the original draft, which was reviewed and edited by CJM, BX, and DSWB.

Conflicts of interest

Danielle. S. W. Benoit is a co-founder and Chief Executive Officer (CEO) of AsteriaRx, a biotechnology company that is developing technology related to the DDS technology described in this manuscript. This interest has been disclosed and is being managed in accordance with the University of Oregon conflict of interest policies. All other authors declare no competing interests.

Data availability

The original contributions presented in the study are included in the article and are supported by information in the supplementary information (SI). Supplementary information: NMR spectra of the polymer (proton and carbon), physicochemical characteristics of SCP-NPs, individual amino acid sources, peptide characteristics, primer sequences, and supporting flow

cytometry and gene expression data. See DOI: https://doi.org/10.1039/d5nh00503e.

Further inquiries can be directed to the corresponding author.

Acknowledgements

This work was supported by grants from the National Institutes of Health (NIH) (R21 AG072692, R01AR064200, R21AR081063, UG3AG097136 to DSWB and T32HD007348 to CJM) and the National Science Foundation (NSF) (CBET-1450897 and DMR-2103553 to DSWB) and from the Center for Translational Biomedical Research Fellowship (CTBR), Peace Health and the University of Oregon (Phil and Penny Knight Campus for Accelerating Scientific Impact) to VR. The authors would like to thank the Genomics & Cell Characterization Core Facility at the University of Oregon for access to MALDI, qPCRs, and confocal microscopy.

References

1 A. M. Phillips, *Injury*, 2005, **36**, 55–57.
2 J.-M. Kim, C. Lin, Z. Stavre, M. B. Greenblatt and J.-H. Shim, *Cells*, 2020, **9**, 2073.
3 B. Ganse, *Front. Immunol.*, 2024, **15**, 1384783.
4 L. Steppe, M. Megafu, M. E. A. Tschaffon-Müller, A. Ignatius and M. Haffner-Luntzer, *Bone Rep.*, 2023, **19**, 101686.
5 G. M. Calori, W. Albisetti, A. Agus, S. Iori and L. Tagliabue, *Injury*, 2007, **38**, S11–S18.
6 P.-L. Chung, S. Zhou, B. Eslami, L. Shen, M. S. LeBoff and J. Glowacki, *J. Cell. Biochem.*, 2014, **115**, 1412–1419.
7 J. Bi, C. Zhang, C. Lu, C. Mo, J. Zeng, M. Yao, B. Jia, Z. Liu, P. Yuan and S. Xu, *J. Autoimmun.*, 2024, **143**, 103169.
8 J. Wagner, S. Schmidt, M. Dadras, J. Huber, C. Wallner, S. Dittfeld, M. Becerikli, H. Jaurich, F. Reinkemeier, M. Drysch, M. Lehnhardt and B. Behr, *J. Trans. Med.*, 2019, **17**, 416.
9 J. Schira, M. Schulte, C. Döbele, C. Wallner, S. Abraham, A. Daigeler, U. Kneser, M. Lehnhardt and B. Behr, *J. Cell. Mol. Med.*, 2015, **19**, 2842–2850.
10 W. Da, L. Tao and Y. Zhu, *Front. Endocrinol.*, 2021, **12**, 675385.
11 H. Wang, T. Yuan, Y. Wang, C. Liu, D. Li, Z. Li and S. Sun, *Aging Cell*, 2024, **23**, e14092.
12 M. M. McDonald, A. S. Kim, B. S. Mulholland and M. Rauner, *JBMR Plus*, 2021, **5**, e10539.
13 N. Ayub, M. Faraj, S. Ghatan, J. A. A. Reijers, N. Napoli, L. Oei, N. Ayub, M. Faraj, S. Ghatan, J. A. A. Reijers, N. Napoli and L. Oei, *J. Clin. Med.*, 2021, **10**, 3002.
14 E. Lewiecki, T. Blicharski, S. Goemaere, K. Lippuner, P. Meisner, P. Miller, A. Miyauchi, J. Maddox, L. Chen and S. Horlait, *J. Clin. Endocrinol. Metab.*, 2018, **103**, 3183–3193.
15 H. Rouco, P. García-García, E. Briffault and P. Diaz-Rodriguez, *Wiley Interdiscip. Rev.: Nanomed. Nanobiotechnol.*, 2023, **15**, e1885.
16 D. Heo, W. Ko, H. Moon, H. Kim, S. Lee, J. Lee, M. Bae, J. Yi, Y. Hwang, J. Bang, E. Kim, S. Do and I. Kwon, *ACS nano*, 2014, **8**, 12049–12062.
17 D. Lee, D. Heo, H. Kim, W. Ko, S. Lee, M. Heo, J. Bang, J. Lee, D. Hwang, S. Do and I. Kwon, *Sci. Rep.*, 2016, **6**, 27336.
18 M. Li, S. Fu, Z. Cai, D. Li, L. Liu, D. Deng, R. Jin and H. Ai, *Regen. Biomater.*, 2021, **8**, rbab027.
19 J. Liu, L. Dang, D. Li, C. Liang, X. He, H. Wu, A. Qian, Z. Yang, D. Au, M. Chiang, B. Zhang, Q. Han, K. Yue, H. Zhang, C. Lv, X. Pan, J. Xu, Z. Bian, P. Shang, W. Tan, Z. Liang, B. Guo, A. Lu and G. Zhang, *Biomaterials*, 2015, **52**, 148–160.
20 C. Jing, B. Li, H. Tan, C. Zhang, H. Liang, H. Na, S. Chen, C. Liu and L. Zhao, *ACS Appl. Bio Mater.*, 2021, **4**, 4907–4916.
21 C. H. Tonk, S. H. Shoushrah, P. Babczyk, B. E. Khaldi-Hansen, M. Schulze, M. Herten and E. Tobiasch, *Int. J. Mol. Sci.*, 2022, **23**, 1393.
22 Y. Wang, M. R. Newman, M. Ackun-Farmmer, M. P. Baranello, T.-J. Sheu, J. E. Puzas and D. S. W. Benoit, *ACS Nano*, 2017, **11**, 9445–9458.
23 B. Xiao, Y. Liu, I. Chandrasiri, E. Adjei-Sowah, J. Mereness, M. Yan and D. S. W. Benoit, *Small*, 2024, **20**, e2305336.
24 I. Chandrasiri, Y. Liu, E. Adjei-Sowah, B. Xiao and D. S. W. Benoit, *Front. Biomater. Sci.*, 2022, **1**, 1003172.
25 J. J. Benvenuta-Tapia, E. Vivaldo-Lima, J. A. Tenorio-López, M. D. L. Á. Vargas-Hernández and H. Vázquez-Torres, *Thermochim. Acta*, 2018, **667**, 93–101.
26 M. Rätzsch, *Prog. Polym. Sci.*, 1988, **13**, 277–337.
27 E. Chernikova, P. Terpugova, C. Bui and B. Charleux, *Polymer*, 2003, **44**, 4101–4107.
28 Z. Yao, J. S. Zhang, M. L. Chen, B. J. Li, Y. Y. Lu and K. Cao, *J. Appl. Polym. Sci.*, 2011, **121**, 1740–1746.
29 E. Adjei-Sowah, V. Rangasami, A. E. Loiselle and D. S. W. Benoit, *ACS Appl. Mater. Interfaces*, 2024, **16**, 68864–68876, DOI: 10.1021/acsami.4c13388.
30 D. E. Maridas, E. Rendina-Ruedy, P. T. Le and C. J. Rosen, *J. Visualized Exp.*, 2018, e56750, DOI: 10.3791/56750.
31 T. Patiño, J. Soriano, L. Barrios, E. Ibáñez, C. Nogués, T. Patiño, J. Soriano, L. Barrios, E. Ibáñez and C. Nogués, *Sci. Rep.*, 2015, **5**, 1.
32 P. S. Gilmour, P. J. O'Shea, M. Fagura, J. E. Pilling, H. Sanganee, H. Wada, P. F. Courtney, S. Kavanagh, P. A. Hall and K. J. Escott, *Toxicol. Appl. Pharmacol.*, 2013, **272**, 399–407.
33 P. A. Hulley and H. J. Knowles, *Cells*, 2022, **11**, 3973.
34 T. Jiang, T. Xia, F. Qiao, N. Wang, Y. Jiang, H. Xin, T. Jiang, T. Xia, F. Qiao, N. Wang, Y. Jiang and H. Xin, *Int. J. Mol. Sci.*, 2023, **24**, 16175.
35 T. Miyazaki, S. Miyauchi, T. Anada, H. Imaizumi and O. Suzuki, *Anal. Biochem.*, 2011, **410**, 7–12.
36 K. Sasagawa, H. Domon, S. Hirayama, T. Maekawa, T. Isono, K. Tabeta and Y. Terao, *Commun. Biol.*, 2025, **8**, 760.
37 S. X. Ge, E. W. Son, R. Yao, S. X. Ge, E. W. Son and R. Yao, *BMC Bioinform.*, 2018, **19**, 1.
38 M. I. Love, W. Huber, S. Anders, M. I. Love, W. Huber and S. Anders, *Genome Biol.*, 2014, **15**, 12.

39 B. Xiao, Y. Liu, I. Chandrasiri, C. Overby and D. S. W. Benoit, *ACS Appl. Mater. Interfaces*, 2023, **15**, 13993–14004, DOI: 10.1021/acsami.2c22471.
40 M. P. Baranello, L. Bauer, C. T. Jordan and D. S. W. Benoit, *Cell. Mol. Bioeng.*, 2015, **8**, 455–470.
41 M. P. Baranello, L. Bauer and D. S. W. Benoit, *Biomacromolecules*, 2014, **15**, 2629–2641, DOI: 10.1021/bm500468.
42 M. R. Newman, S. G. Russell, C. S. Schmitt, I. A. Marozas, T.-J. Sheu, J. E. Puzas and D. S. W. Benoit, *Biomacromolecules*, 2017, **19**, 71–84.
43 J. Dolai, K. Mandal and N. R. Jana, *ACS Appl. Nano Mater.*, 2021, **4**, 6471–6496.
44 F. Afhkami, P. Ahmadi and G. Rostami, *Clin. Exp. Dent. Res.*, 2025, **11**, e70075.
45 S. C. Marks, *J. Oral Pathol. Med.*, 1983, **12**, 226–256.
46 T. Yi, H.-J. Kim, J.-Y. Cho, K. M. Woo, H.-M. Ryoo, G.-S. Kim and J.-H. Baek, *Biochem. Biophys. Res. Commun.*, 2006, **347**, 178–184.
47 V. Parthasarathy, F. Martin, A. Higginbottom, H. Murray, G. W. Moseley, R. C. Read, G. Mal, R. Hulme, P. N. Monk and L. J. Partridge, *Immunology*, 2009, **127**, 237–248.
48 P. A. Hulley, H. J. Knowles, P. A. Hulley and H. J. Knowles, *Cells*, 2022, **11**, 3973.
49 T. Jiang, T. Xia, F. Qiao, N. Wang, Y. Jiang and H. Xin, *Int. J. Mol. Sci.*, 2023, **24**, 16175.
50 A. E. Grigoriadis, Z.-Q. Wang, M. G. Cecchini, W. Hofstetter, R. Felix, H. A. Fleisch and E. F. Wagner, *Science*, 1994, **266**, 443–448.
51 T. Miyamoto, *Keio J. Med.*, 2011, **60**, 101–105.
52 S. Lotinun, R. Kiviranta, T. Matsubara, J. A. Alzate, L. Neff, A. Lüth, I. Koskivirta, B. Kleuser, J. Vacher, E. Vuorio, W. C. Horne and R. Baron, *J. Clin. Invest.*, 2013, **123**, 101–105.
53 H. Wu, G. Xu and Y.-P. Li, *J. Bone Miner. Res.*, 2008, **24**, 871–885.
54 M. Amirhosseini, R. Madsen, K. Escott, M. Bostrom, F. Ross and A. Fahlgren, *J. Cell. Physiol.*, 2018, **233**, 2398–2408.
55 M. Arioka, F. Takahashi-Yanaga, M. Sasaki, T. Yoshihara, S. Morimoto, M. Hirata, Y. Mori and T. Sasaguri, *Biochem. Pharmacol.*, 2014, **90**, 397–405.
56 Y. Kobayashi, S. Uehara and N. Udagawa, *J. Oral Biosci.*, 2018, **60**, 31–35.
57 G. Han, J. Zuo and L. S. Holliday, *Biomolecules*, 2019, **9**, 17.
58 I. Song, J. H. Kim, K. Kim, H. M. Jin, B. U. Youn and N. Kim, *FEBS Lett.*, 2009, **583**, 2435–2440.
59 Z.-Y. Guo, N.-N. Yin, X.-F. Li, M.-M. Wang, X.-N. Sui, C.-D. Jiang, M.-H. Xu, X.-E. Jia, C.-J. Fu, T.-L. Chen and X. Liu, *Tissue Cell*, 2025, **93**, 102645.
60 T. Yamaguchi, A. Movila, S. Kataoka, W. Wisitrasameewong, M. R. Torruella, M. Murakoshi, S. Murakami and T. Kawai, *Infect. Immun.*, 2016, **84**, 2802–2812.
61 A. R. Hayman, A. J. Bune and T. M. Cox, *J. Anat.*, 2000, **196**, 433–441.
62 I. R. Nedeva, M. Vitale, A. Elson, J. A. Hoyland and J. Bella, *Front. Cell Dev. Biol.*, 2021, **9**, 641162.
63 P. E. Purdue, T. N. Crotti, Z. Shen, J. Swantek, J. Li, J. Hill, A. Hanidu, J. Dimock, G. Nabozny, S. R. Goldring, K. P. McHugh, P. E. Purdue, T. N. Crotti, Z. Shen, J. Swantek, J. Li, J. Hill, A. Hanidu, J. Dimock, G. Nabozny, S. R. Goldring and K. P. McHugh, *Sci. Rep.*, 2014, **4**, 1.
64 A. Jura-Półtorak, A. Szeremeta, K. Olczyk, A. Zoń-Giebel and K. Komosińska-Vassev, *J. Clin. Med.*, 2021, **10**, 2905.
65 A. Nakamura, Y. Dohi, M. Akahane, H. Ohgushi, H. Nakajima, H. Funaoka and Y. Takakura, *Tissue Eng., Part C*, 2009, **15**, 169–180.
66 M. M. Weivoda, C. K. Chew, D. G. Monroe, J. N. Farr, E. J. Atkinson, J. R. Geske, B. Eckhardt, B. Thicke, M. Ruan, A. J. Tweed, L. K. McCready, R. A. Rizza, A. Matveyenko, M. Kassem, T. L. Andersen, A. Vella, M. T. Drake, B. L. Clarke, M. J. Oursler, S. Khosla, M. M. Weivoda, C. K. Chew, D. G. Monroe, J. N. Farr, E. J. Atkinson, J. R. Geske, B. Eckhardt, B. Thicke, M. Ruan, A. J. Tweed, L. K. McCready, R. A. Rizza, A. Matveyenko, M. Kassem, T. L. Andersen, A. Vella, M. T. Drake, B. L. Clarke, M. J. Oursler and S. Khosla, *Nat. Commun.*, 2020, **11**, 1.

